Investigating soil erosion vulnerable zones based on clustered geoinformatics approach: a case study of Tyume River Catchment, Eastern Cape, South Africa

Investigación de las zonas vulnerables a la erosión del suelo basada en un enfoque geoinformático agrupado: un estudio de caso de la cuenca del río Tyume, Cabo Oriental, Sudáfrica

Mbatyoti, S.[(a)*]; Sumner, P.[(a)]; Kalumba, A. M.[(a,b)]; Owolabi, S. T.[(c)]; Belle, J. A.[(c)]

(a) Department of Geography and Environmental Sciences, Faculty of Science and Agriculture, University of Fort Hare, Private Bag X1314, Alice, 5700, Eastern Cape, South Africa.
(b) Geospatial Application, Climate Change and Environmental Sustainability Lab–GACCES, University of Fort Hare, Private Bag X1314, Alice 5700, Eastern Cape Province, South Africa.
(c) Disaster Management Training and Education Centre for Africa, Faculty of Natural and Agricultural Sciences, University of the Free State.
* styoti85@gmail.com; Tel.: +27-81-490-6068

Abstract

Rigorous field surveys, environmental specificity, and data paucity hamper detailed soil erosion assessments, model selection, ecological monitoring, and prioritization against soil erosion. To address this in a topographically complex environment, the present study presents a novel selection of physiographic factors integrated geospatially with the land use/cover and geology data to prioritize the soil erosion vulnerable areas within a watershed, using Tyume River Catchment, Eastern Cape, South Africa as a case study. A quantitative morphometric analysis involving parameters such as the drainage density, topographic wetness index, terrain ruggedness index, topographic position index, and vector roughness measure was computed using a digital elevation model based on their inference of watershed's morphogenetic response to anthropic factors and pluviometric processes. Based on expert judgment for thematic ranking and weightage, the soil erosion prioritization area map was generated through weighted overlay analysis of the morphometric parameters with land use land cover and surficial lithology themes. The results depicted a catchment-scale soil erosion vulnerability map, classified into very high (40 km²), high (135 km²), medium (209 km²), low (186 km²), and non-vulnerable (113 km²) zones. Using Google Earth image analyses through the coefficient of determination (R^2 = 0.563) and Receiver Operating Characteristics Curve (AUC = 0.899), the model corroboration indicated that the soil erosion vulnerability assessment is reliable and highly predictive. The study identified free-range animal operation and hillslope overgrazing, especially in riparian zones, as the environmental practices ag-

gravate the catchment's terrain susceptibility to soil erosion. The assessment showed that some of the selected morphometric parameters could be used to improve the validated soil erosion models in mountainous regions. Due to the high precision of the engaged approach and the identified environmental concerns, the method can be adopted in similar environments.

Key words: Landscape indices, Soil erosion, Vulnerability, Morphometric analysis, South Africa.

Resumen

El exhaustivo trabajo de campo, la especificidad medioambiental y la escasez de datos dificultan las evaluaciones detalladas de la erosión del suelo, la selección de modelos, el seguimiento ecológico y la priorización de la lucha contra la erosión del terreno. Para abordar este problema en un entorno topográficamente complejo, el presente estudio presenta una nueva selección de factores fisiográficos integrados geoespacialmente con los datos de uso / cobertura de la tierra y geología para priorizar las zonas vulnerables a la erosión del suelo dentro de una cuenca hidrográfica, aplicado a la cuenca del río Tyume, Sudáfrica como un estudio de caso. Se calculó un análisis morfométrico cuantitativo que incluía parámetros como la densidad de drenaje, el índice de humedad topográfica, el Índice de rugosidad del terreno, el indicador de la posición topográfica y la medida de rigidez del vector, utilizando un modelo de elevación digital basado en su inferencia de la respuesta morfogenética de la capa de agua a los factores antropogénicos y los procesos pluviométricos. Sobre la base del juicio de expertos para la clasificación temática y la ponderación, se generó el mapa de prioridad de la erosión del suelo a través de un análisis ponderado de la superposición de los parámetros morfométricos con la cobertura de las tierras de uso de la tierra y las capas de la litología superficial. El resultado mostró un mapa de la vulnerabilidad a la erosión del suelo a escala de cuenca, clasificado en zonas muy altas (40 km^2), altas (135 km^2), medianas (209 km^2), bajas (186 km^2) y no vulnerables (113 km^2). Utilizando los análisis de imágenes de Google Earth a través del coeficiente de determinación ($R^2 = 0,563$) y la curva de características operacionales del receptor (AUC = 0,899), la corroboración del modelo indicó que la evaluación de la vulnerabilidad a la erosión del suelo es fiable y altamente predictiva. El estudio identificó la explotación extensiva de animales y el sobrepastoreo de las colinas, particularmente en las zonas ribereñas, ya que las prácticas ambientales agravan la susceptibilidad del terreno de la cuenca a la erosión del suelo. La evaluación mostró que algunos de los parámetros morfométricos seleccionados podrían utilizarse para mejorar los modelos validados de erosión del suelo en las regiones montañosas. Debido a la alta precisión del enfoque empleado y las afecciones ambientales identificadas, el método puede adoptarse en entornos similares.

Palabras clave: Índices de paisaje, Erosión del suelo, Vulnerabilidad, Análisis morfométrico, Sudáfrica.

1. Introducción

Soil erosion is a severe environmental concern due to its detrimental effect on ecological productivity, soil hydrological processes, and the threat to the landscape's viability for agriculture (He *et al.*, 2024). Currently, soil erosion research has become relevant on the local and international agendas to address ongoing stream siltation, streamflow reduction, water resources pollution, and the abatement of water infrastructure functionality (Martín-ez-Murillo *et al.*, 2011; DWS, 2017; Schillaci *et al.*, 2023). For example, dam sedimentation has rendered several large dams in the Eastern Cape of South Africa efficient (DWS, 2017; Basson *et al.*, 2022), leading to a rise in water and food insecurity. Soil erosion has led to increased land abandonment, endangering ecological services, the conservation of natural resources, and the sustainability of the environment globally (Sibiya *et al.*, 2023; Shtober-Zisu *et al.*, 2024). Globally, one-eighth of the world's population is at risk due to land

degradation, while one-quarter are directly affected (Smith *et al.*, 2020). In the last ten years, land degradation and soil erosion have caused more than 80,000 km² of farmland to lose about 10 to 40 tons/hectare due to land degradation and soil erosion in the recent decade (Hladky *et al.*, 2017) while the rate of soil loss was noted to be twice the rate of soil formation annually (Parwada and Van Tol, 2016). Consequently, the erosion of the topsoil layer will become a severe environmental issue, especially in regions sensitive to climate change (Owolabi and Belle, 2023).

The vulnerability of soil to erosion in South Africa is high due to the effect of climate change, slope steepness, soil/geologic type, and increased extent of change of land use/cover (Owolabi *et al.*, 2022). This study undertakes an integrated assessment of land degradation by soil erosion driven by water at a catchment scale. Many soil erosion models have been developed to monitor and evaluate the extent and potential impacts of water soil erosion, such as Universal Soil Loss Equation (USLE) (Wischmeier and Smith, 1978; Helmi, 2023), Water Erosion Prediction Project (WEPP) (Flanagan and Nearing, 1995; Ugwu *et al.*, 2024), Soil and Water Assessment Tool (SWAT) (Arnold *et al.*, 1998; Aloui *et al.*, 2023), and European Soil Erosion Model (EUROSEM) (Morgan *et al.*, 1998; Busico *et al.*, 2023). The proposition of several soil erosion models is mainly due to the variation in geohydrological processes and watershed response due to the varying physiographic factors influencing terrain susceptibility to soil erosion. Hence, the USLE was modified to Revised Universal Soil Loss Equation (RUSLE) (Renard *et al.*, 1991) and subsequently modified to Sediment Assessment Tool for Effective Erosion Control (SATEEC) for site-specific soil loss estimation (Mhangara *et al.*, 2012). However, most models are data-intensive, requiring rigorous field assessment for soil samples, terrain in-situ testing, and extensive field coverage,

which could be unsafe, labor-intensive, costly, timeous, and require detailed laboratory assessment. However, the local climatic activities, geohydrological processes, soil intrinsic properties, and land cover change effects are depicted on the morphogenetic imprints of the watershed, which can be easily mapped through quantitative morphometric analysis (Bhatt and Ahmed, 2014; Jadidoleslam *et al.*, 2019; Deribew *et al.*, 2024; Vieira and Oyguc, 2024). As a result, this study presents an integrated morphometric-based approach to address the gap in model-site specificity.

Increasing awareness of terrain and morphometric characteristics has helped improve watershed management (Bhatt and Ahmed, 2014). Morphometric parameter (MPs) analysis provides information on the soil surface conditions, soil thickness (Deribew *et al.*, 2024), and fluid/ moisture transfer function associated with runoff production (Jadidoleslam *et al.*, 2019). Terrain information drawn from MPs includes drainage density (DD), topographic wetness index (TWI), terrain ruggedness index (TRI), topographic position index (TPI), and vector roughness measure (VRM). TWI models the influence of hillslope factors on soil water transport (Zhang *et al.*, 2024), and TRI projects the areas of high potential for overland flow (high TRI) and depressions (low TRI) (Amatulli *et al.*, 2020). TPI calibrates the runoff-contributing areas within a watershed (Avand *et al.*, 2022). VRM computes the relative positions of geomorphic incisions influenced by gravity, soil surface condition, and hydrographic network (Smith, 2014). DD depicts the drainage areas with high susceptibility to detachment when combined with other soil/ terrain parameters (Jadidoleslam *et al.*, 2019). MPs have been unilaterally adopted and hybridized with a land use/ land cover map using a multi-criteria classifier to prioritize areas of soil erosion (Haokip *et al.*, 2022). The effectiveness of MPs can be improved by integrating its themes with signif-

icant land use/ cover (LU/C) features and geology, thereby addressing the research gap on the relevant geomorphic-based soil erosion models in terrain with complex topography. As a result, the study proposed a Soil Erosion Potential Area (SEPA) model based on the weighted overlay computation of themes of five MPs with a land use/ cover map and surficial lithology themes guided by expert decisions drawn from extensive qualitative literature review and content analysis to score the relative erosional influence of the selected themes. The proposition of SEPA is motivated by Sharma's (2010) selection of morphometric parameters (3), TWI, slope length factor, and stream power index, alongside an inverted NDVI, which are integrated using overlay analysis after ISODATA clustering. SEPA computation is based on the conventional approach of the multi-parametric decision method expressed as a weighted linear combination in Pal (2016) and Ghosh and Lepcha (2019) soil erosion studies. The geospatial-assisted delineations of the environments involving multi-parametric decision-making have been widely adopted in other environmental studies such as groundwater exploitation (Hasanuzzaman *et al.*, 2022; Dimple *et al.*, 2023), landslide investigation (Arumugam *et al.*, 2023), and wildfire studies (Djabri *et al.*, 2023), as conceptualized in SEPA computation here. To this end, the study is outlined to address the following research questions; (a) Can a soil erosion model mainly based on morphometric assessment among others, provide a reliable qualitative vulnerability assessment? (b) What are the convent factors driving soil erosion in a topographic domain.

The research aims to present an integrated framework model of soil erosion assessment based on the analysis of geo-morphometric parameters, land use/cover, and geological factors in the Tyume River Basin. The study is addressed using two central objectives, which include: (1) the geospatial mapping and integration of Tyume river basin morphometric parameters with land use/cover and geology themes, and (2) a critical investigation of the ground situation aided by Google Earth for thorough visualization and erosion proneness estimation for soil erosion model corroboration using receiver operating curves and confusion matrices to enhance the qualitative interpretation of areas vulnerable to soil erosion. By presenting this geomorphic-based integrated approach, this study contributes to the body of knowledge on the suitability of MPs in optimizing soil erosion models in areas with complex topography.

2. Materials and methods

2.1. Description of the study area

The Tyume River catchment covers an area of 642.37 km² and an altitudinal range of 308 - 1826 m.a.s.l. (Figure 1). The catchment is located at the headwater of Keiskamma watershed, in Amathole municipality, Eastern Cape, South Africa. It has an average winter temperature of 11°C which ranges between -4°C and 15°C in the winter (Jun-Jul-Aug), and an average summer temperature of 20°C which ranges between 17°C and 38°C in summer (Dec-Jan-Feb). The catchment is characterized by a mean annual rainfall of 450 mm – 600 mm, with extreme rainfall experienced at the higher altitudes where the terrain topography possibly influences the rainfall at the north section of the Tyume (Owolabi *et al.*, 2021a). The mean monthly discharge of Tyume River ranges from 8.11 to 33.41 m³/s with the highest in March and the lowest in July while the mean annual discharge is estimated at 235 m³/s using the last 44 years streamflow data. Tyume River is 75 km long and runs southward from the Hogsback State Forest at the north, through Alice, the center, and several rural settlements to the outlet where its confluences into the Keiskamma River, the tertiary catchment at the south,

where Tyume catchment positions as a head-water (Figure 1).

The landform in the Tyume basin can be classified as sub-range hilly terrain at the extreme north as a part of the Great Escarpment and flanking the west-northwest-north-northeast-east and the peneplain that depresses to the foothill in the south (Dijkshoorn *et al.*, 2008). The catchment is geologically underlain by the dominant Tatarian arenaceous argillites of Balfour Formation, the subordinate Kazanian Light Grey sandstone of Middleton Formation at the extreme South, and the Scythian argillaceous arenites of Katberg Formation, with the Beaufort Group and the Karoo Supergroup (Owolabi *et al.*, 2021b). The dominant soil fractions are Calcic Vertisols at the north, Calcaric Regosols at the center, and coarse deposits in the south (Dijkshoorn *et al.*, 2008). The natural vegetation of the area is classified into three significant biomes: dense forest (north extreme at Hogsback), savanna (center to the west), and tropical thicket (center to the east and south). Visual inspection within the terrain and Google Earth inspection showed vivid evidence of onsite effect of soil erosion, degenerating into a badlands while the offsite effects where manifested through periodic siltation of Tyume River and sedimentation at the plain by the south of the catchment.

2.2. Data sourcing and pre-processing

A digital elevation model (DEM) with a 30 m by 30 m resolution, provided by the Shuttle Radar Topographic Mission (SRTM) and the Landsat 8 Operation Land Imager (OLI) data were downloaded from the USGS Earth Explorer website (https://earthexplorer.usgs.gov/) and the geology map obtained from Council for Geoscience Studies (CGS). The winter month OLI (July 2019) was selected due to low rainfall intensity, wind speed, and cloud cover, enabling a quality raster's spec-
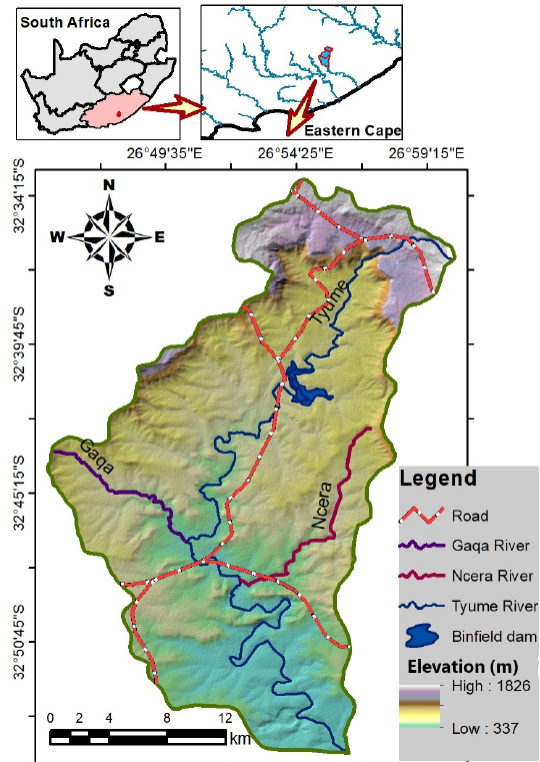

Figure 1. Tyume River basin showing the main river valley, Tyume tributaries, and elevation.

Figura 1. Cuenca del río Tyume que muestra el valle principal del río, los afluentes del Tyume y la elevación.

tral reflectance. The DEM was pre-processed to avoid radiometric errors and ensure atmospheric correction in PCI Geomatica 2015. Data relevant to geology, anthropic factors, and pluviometric information such as the drainage density (DD), topographic wetness index (TWI), topographic position index (TPI), and terrain ruggedness index (TRI), vector roughness measure (VRM) were clipped or computed.

Each layer was qualitatively classified after collating the input data layers by assigning the relative weighting values to each unit factor based on field knowledge (Google Earth inspection) and literature. A priority zoning based on the relative significance of factors influencing soil erosion by water in the study terrain was used to develop a rating system to
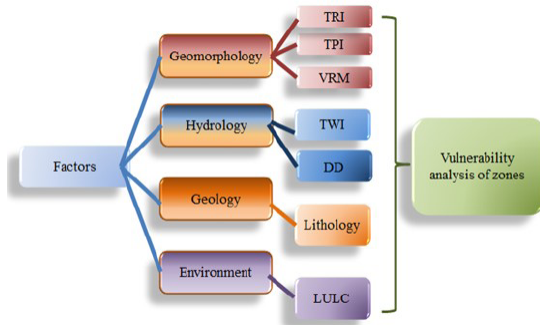
Figure 2. Classification scheme for the projected Topographic Wetness Index (Owolabi *et al.*, 2020).

Figura 2. Esquema de clasificación para el Índice de Humedad Topográfica proyectado (Owolabi et al., 2020).

ensure a qualitative map combination (Sarkar and Kanungo, 2004). The approach engaged in this study may be specific to a complex terrain such as found in Hogsback escarpment of South Africa. The methodology involved factors selection, data clustering in a GIS platform, computation of soil erosion potential zones, and corroboration of the vulnerability map and the DEM data by ground-truthing. The study was further corroborated using Google Earth scenery mapping in Google Earth Pro software (Farhan and Nawaiseh, 2015), coefficient of determination, and receiver operating characteristic curve. The conceptual approach that guides the production of soil erosion by water vulnerability map is presented in Figure 2.

2.3. Preparation and computation of the thematic layers

2.3.1. Drainage density

The DEM was processed for watershed delineation by converting the raw DEM raster into fil (a geodatabase file) data. Flow direction was generated from the fil raster and further processed for the drainage accumulation track. The resulting accumulation raster was refined for drainage tracks not to be less than 100 units per path inflection (DEM ridge-line). The sink, snap pour point, and stream links were computed for stream order computation. Computation of the stream order was carried out using the Strahler approach (Strahler, 1957). The resulting stream order was converted from raster into polylines and a drainage density map in ArcMap 10.8.1 (Owolabi *et al.*, 2020). The resulting featured class raster is classified into five according to Table 1 (Owolabi *et al.*, 2020).

Table 1. Classification scheme for Tyume drainage density map (Owolabi *et al.*, 2020).

Tabla 1. Esquema de clasificación para el mapa de densidad de drenaje de Tyume (Owolabi et al., 2020).

Class name and rate	Range of Drainage density
Very low	0 – 150
Low	151 – 240
Moderate	241 – 360
High	361 – 600

2.3.2. Topographic Wetness Index

The topographic wetness index (TWI) was generated from the elevation map extracted from ASTER DEM in ArcMap 10.8.1. The study area DEM raster was processed to create the slope map in ArcMap. The output measurement was carried out in degree format at the Z factor of 1 (at default) to reduce the influence of variogram overestimation. Calculation of the TWI was carried out in the raster calculator, using equation 1 (Kirkby and Statham, 1975; Hojati and Mokarram, 2016);

$$TWI = \ln\left[\frac{a}{tan(\beta)}\right] \qquad (1)$$

Where α, specific catchment area = catchment area, A, per unit contour length, L, (A/L), and $tan(\beta)$ = slope. However, the TWI was converted into an integer format to classify the zones of *TWI* within the upper and lower quartile to enable the projection of the zones of high and low *TWI*. The resulting projection of *TWI* spots was classified into four according to Table 2 (Owolabi *et al.*, 2020).

Table 2. Classification scheme for the projected Topographic Wetness Index (Owolabi *et al.*, 2020).

Tabla 2. Esquema de clasificación para el Índice de Humedad Topográfica proyectado (Owolabi et al., 2020).

Class name	Range of values of TWI
High TWI	6.3 – -12.7
Steep hillslope	-12.8 – -14.4
Gentle zone	-14.5 – -16.6
Low TWI	-16.7 – -20.5

2.3.3. Terrain ruggedness index

Terrain ruggedness index (*TRI*) was carried out by computing the square of the summation of grid cell difference relative to its neighboring cell at the scale of 75 m, where a slight elevation change can be significant. *TRI* is based on the equation of Riley *et al.* (1999) as presented in equation 2:

$$TRI = (\Sigma(Z_c - Z_i)^2)^2 \qquad (2)$$

Where;

Z_c = elevation of a central cell

Z_i = elevation roughness measure n of each cell in the neighborhood at the scale of 75 m i = 1, 2,..., 8.

2.3.4. Topographic position index

The topographic position index is based on equation 3, formulated by Weiss (2001) and modified by Jennes (2006):

$$TPI = Z_0 - \Sigma_{n-1}(Z_0/n) \qquad (3)$$

Where;

Z_c = elevation of a focal cell

Z_n = elevation of integrated neighborhood cells within the scale of 75m

n = The total number of the neighboring cells around the focal cell.

2.3.5. Vector roughness measure

The vector roughness measure estimation is based on calculating slope variability as a 3-dimensional attribute of vertical and horizontal aspect components. Hence, the slope and the Aspect of the study area are computed first. It is based on standard trigonometric operation according to the steps as presented in equation 4 (Sappington *et al.*, 2007):

$$VRM = 1 - \left(\sqrt{X_{sum}^2 + Y_{sum}^2 + Z_{sum}^2} \right)/75^2 \qquad (4)$$

Where;

$$X_{sum} = Focal(\sin A, \oint = sum)$$
$$Y_{sum} = Focal(\cos A, \oint = sum)$$
$$Z_{sum} = Focal(\cos \int, \oint = sum)$$

A = Aspect, $\int$ = slope, and $\oint$ = interface function, while 75 m represents the scale of computation.

2.3.6. Land use / cover and accuracy assessment

The bands 1, 2, 3, 4, 5, 6, and 7 of Landsat 8 OLI were exported into ArcMap 10.8.1 and stacked to obtain a composite band. The change in the computation of land use /land cover (LU/C) adopted the supervised mapping approach. For developing a training manager sample for the computation exercise, the false-color composite bands for vegetation, water bodies, and built-up areas were computed using the information presented in Table 3.

At least 20 return-on-investment training samples were randomly selected per three cells for every tonal variation in areas with a concentration of spectral reflectance. However, points chosen for the training manag-

er samples matched historical images of the study area acquired from the Google Earth map. The LU/C computation was based on the five significant features with high sensitivity to soil erosion processes (Table 4).

Table 3. Band selection and arrangement for land use/ land cover characterization (Butler, 2013).

Tabla 3. Selección y disposición de bandas para la caracterización del uso/cobertura del suelo (Butler, 2013).

Composite feature	Band combination used
Natural color	4 3 2
Built-up areas	7 6 4
Woodland	5 6 2
Scrubs and velds	6 5 2
Water bodies/bare	5 6 4

A signature file was generated following the characterization of false-color composite band reflectance. The supervised raster characterization was mapped using a maximum likelihood approach at an equal priority probability weighting. The image classification accuracy for respective years of the LULC was performed with 72 samples using the confusion matrix. The confusion matrix was computed by sampling 72 training cells randomly as the user's value on the LULC. The sample is compared with a Google Earth Pro image of the same time slide and recorded as the producer's value.

The overall accuracy and the Kappa coefficient are calculated as shown in equations 5 and 6:

$$Overall\ Accuracy = \frac{\text{The sum of Correctly classified pixels}}{\text{Total number of reference pixels}} \times 100 \quad (5)$$

$$K = \frac{N(\sum_{i=1}^{r} x_{ii}) - (\sum_{i=1}^{r}(x_{i+} \times x_{+i}))}{N^2 - (\sum_{i=1}^{r}(x_{i+} \times x_{+i}))} \quad (6)$$

where *r* is the number of rows in the error matrix, x_{ii} is the classified pixels in row *I* and column *I*, x_{i+} and x_{+i} are the pixels in row *I* and column *I,* and *N* is the total number of the sampling points used.

The overall classification accuracy and the Kappa coefficient value for the resultant error matrix of the computed LU/C showed a near-perfection deduction, with the overall accuracy and Kappa coefficient being 86.11% and 82.49% (Table 5). The user's value is computed along the rows, while the producer's value is calculated along the column.

The reflectance distribution was classified as values, while the characteristic cells were enumerated as counts in the attribute table, which was extracted for each raster for further statistical estimation.

Table 4. Thematic categories for land use/land cover mapping.

Tabla 4. Categorías temáticas para la cartografía de uso/cobertura del suelo.

LU/C Features	Description
Built-up areas	Areas predominated with artificial imperviousness cover, such as tarred or plastered roads, plastered parks, residential, institutional, and commercial buildings.
Waterbody	Areas with evidence of natural ponds or flow. This includes lakes, dams, open streams, rivers, natural pools, etc.
Woodland	Areas predominated with an advanced stage of tree growth with a possible high vegetation density greater than 50%. This includes areas dominated by thickets, canopy trees, and deciduous trees.
Scrubs and Veld	Areas with sparse shrubs, veld, possible cropping or grazing activities with vegetation density within 20% - 50% and vegetation height, not more than 1.80 m.
Bare-ground	Areas exhibiting signs of severe degradation, clear-cuts, with scanty grass cover and shrubs, untarred (dirt) roads, and with low vegetation density, less than 20%.

Table 5. LULC classification accuracy assessment based on error and confusion matrix.
Tabla 5. Evaluación de la precisión de la clasificación LULC basada en la matriz de error y confusión.

Land Use/ Cover	Built-up area	Bare ground	Forest	Veld	Water body	Total	Comm error	User's accuracy
Built-up area	11	1	0	3	0	15	26.67	73.33
Bare ground	0	15	0	3	0	18	16.67	83.33
Forest	0	0	10	1	0	11	09.09	90.91
Veld	0	1	1	14	0	16	12.50	87.50
Water body	0	0	0	0	12	12	00.00	100
Total	11	17	11	21	12	72		
Omission error	0	11.76	09.09	33.33	0			
Producer's accuracy	100	88.24	90.91	66.67	100			
Overall accuracy (%)	86.11							
Kappa coefficient (%)	82.49							

2.3.7. Geological Spatial distribution

The Eastern Cape geology map (scale 1:250,000) was acquired from the Council for Geoscience Studies (CGS) and modified by extracting the study area. The clipped data was converted into a raster file and reclassified based on the mudstone-sandstone ratio, while dolerite was the most resistant rock among the geologic class. Różycka *et al.* (2017) noted that mudstone-dominated materials are highly susceptible to landslide and mass waste. Hence, this served as a basis for litho-material reclassification for vulnerability mapping. Details of mudstone content in the Eastern Cape Karoo Supergroup are documented in Owolabi *et al.* (2021b).

2.4. Overlay analysis

The maps prepared earlier were reclassified and assigned a weight based on their susceptibility potential. Assignment of weightage was majorly based on review and expert judgment. Hence, VRM was assigned the least weightage (12) while LU/C is rated highest (16) due to its vulnerability tendency at the zones of morphogenetic alteration. DD, TWI, TRI, TPI, and Geology were assigned similar weights (15) (Table 6). The weighted sum method of overlay analysis was employed to compute the vulnerability analysis using the weightage of layers (Table 6) and the proposed Soil Erosion Potential Areas, SEPA, in equation 7;

$$SEPA = \sum_{i=1}^{7}(W_i \times fs_{ij}) \qquad (7)$$

where W_i represents the weight for factor *i* and fs_{ij} Represents the field score of class *j* of factor *i*. The weighted sum approach was built in ArcMap 10.8.1. The SEPA index is classified into five major zones: critically high, high, medium, low, and non-vulnerable soil erosion areas.

2.5. Validation of soil erosion vulnerability map

The assessment was validated using a Google Earth map survey. Unlike field mapping, which may be limited by inaccessibility and coverage, the Google Earth map offers a 3-dimensional view without a restriction to length. Eighty-three spots within the None/very low, low, moderate to high soil erosion zones were georeferenced randomly from the soil ero-

Table 6. Weightage of thematic layer for overlay analysis of vulnerability map production.
Tabla 6. Ponderación de la capa temática para el análisis de superposición de la producción de mapas de vulnerabilidad.

Thematic layer (Weight)	Classes	Field score	Field Weight
Drainage density (15)	Very low	1	1.88
	Ineffective	2	3.75
	Effective	7	13.13
	Ponding	8	15.00
Topographic wetness index (15)	None	1	2.5
	Low	2	5.0
	Moderate	5	12.5
	High	6	15.0
Terrain ruggedness index (15)	Flat	1	3
	Low	2	6
	Moderate	4	12
	High	5	15
Topographic position index (12)	Very low	1	03.75
	Low	4	15.00
	High	5	18.75
	Very high	6	22.50
Vector roughness measure (12)	Very low	1	2.4
	Low	2	4.8
	High	4	9.6
	Very high	5	12
Geology (15)	Jurassic Dolerite	1	2.5
	Quaternary sand	2	5
	Middleton Formation	3	7.5
	Katberg Formation	4	10
	Balfour Formation	6	15
Land use/ land cover (16)	Woodland	1	2
	Scrub and Veld	2	4
	Built-up	5	10
	Water bodies	6	12
	Bare	8	16

sion vulnerability map for visual inspection and analysis under the Google Earth map. The Google Earth time was set to the default (with variation between December 2019 and April 2020) as deployed by CNES/Airbus. The sampling points were carefully randomized across the entire catchment area and tributaries to prevent the monotony of attributes in the river valley (Vrieling *et al.*, 2006). Hence, sampling points are not in the center of the catchment. Information filtered from the use of Google Earth includes the following:

1. Discrimination of erosion channel from a drainage channel.

2. Identification of erosion type.

3. Linear measurement of the erosional path.

4. Extraction of camera height for the resolution of magnification.

5. Classification of slope and bareness of the affected area.

6. Estimation of soil erosion proneness.

The visual interpretation and estimation of Soil erosion proneness using the Google Earth map survey was informed by Dwivedi and Ramana (2003) and Vrieling *et al.* (2006), indicated in equation 8:

$$\text{Ep} = \frac{f_b \times f_s \times M_{rs} (\Sigma N_g + \Sigma N_r + \Sigma N_s)}{100} \quad (8)$$

where Ep is the erosion proneness, f_b is the bareness factor, f_s is the slope factor, M_{rf} is the camera reference scale in km, N_g is the normalized length of a gully in km, N_r is the normalized length of a rill in km, and N_s is the length of the sheet in km. The length of the rill and gully are normalized by the multiples of 2 and 3, respectively, due to the variation in depth of impact. The designation of rating factors based on bareness and the extent of the slope was based on Table 7.

The calculated soil erosion proneness was tabulated with its georeference and the corresponding grid codes for soil vulnerability drawn from georeference identity. The extracted grid codes are plotted against the Ep for its coefficient of determination. Based on the coefficient of determination (R^2), $R^2 < 0.5$ indicates that the model is unreliable and does not replicate the field observation. $R^2 = 0.5$ suggests that the model is reliable as 50% of the field observation correlates with the simulation provided, while $R^2 \geq 0.75$ indicates

that the model is excellent in replicating the field observation.

Table 7. The rating factor is used for calculating erosion proneness.

Tabla 7. El factor de calificación se utiliza para calcular la propensión a la erosión.

Attributes	Rating factors
Bareness	1
Densely riparian	2
Lightly vegetated	3
Veld	4
Bared	5
Peneplain	1
Pediplain	2
Fair hillslope	3
Abrupt hillslope	4

The performance of SEPA was further assessed graphically using the Receiver operating characteristics curves (ROC). ROC is a binary probabilistic algorithm that evaluate model performance by quantifying the coherence of predicted data with the ranked probabilities of the observed data using the plot of model sensitivity against the probable extent of model specificity from 100% (Verbakel *et al.,* 2020; Halder *et al.,* 2021). The model sensitivity estimates the proportion of the positive predictive value (PPV) among the actual noncase, the specificity estimates the proportion of the negative predictive value (NPV) while the area under curve (AUC) provides the goodness of the fit. ROC curve has provided crucial metrics in similar soil erosion susceptibility mapping involving morphometric parameters among others (Hembram *et al.,* 2019; Halder *et al.,* 2021; Biswa and Giri, 2023; Dutta *et al.,* 2024).

The model sensitivity and specificity are obtained using equations 9 and 10:

$$PPV = \frac{TP}{TP+FN} \qquad (9)$$

$$NPV = \frac{FP}{FP+TN} \qquad (10)$$

Where *TP* denotes the true positive, *FN* denotes the false negative, *FP* denotes the false positive, and *TN* denotes the true negative. The model sensitivity and specificity in this study are obtained by classifying the grid-codes into two; from the moderate with low grid-code (Grid-code ≤ 350) and moderate to very high soil erosion (Grid > 350) and extracting the frequencies of higher (lower) E_pE_p, relative to the grid codes about varying scenarios of class threshold and vice-versa. The higher (lower) E_pE_p are cross-tabulated as the significantly (insignificantly) eroded frequencies, against the "Grid > 350" (Grid-code ≤ 350) with the rationale that higher (lower) E_pE_p and "Grid > 350" (Grid-code ≤ 350) cross-tabulation provides the true positive, TP (true negative, TN). The positive likelihood ratio was derived by obtaining the slope of sensitivity/(1-sphericity), while the Area Under Curve (AUC) was obtained by integrating the sensitivity variables over sphericity variables. The optimum threshold was obtained from the outcome resulting in the largest sensitivity and sphericity from the grid codes.

In addition, a fishnet (20 by 20) is created in ArcMap to discretize the entire study area for critical validation. The discreet units produced 400 units, with 1.92 km by 1.13 km, which was further trimmed into 219 units by removing units whose centroids were outside the study portion. The predicted SEPA for each discreet unit was extracted zonal for the dominating (majority) SEPA class. Also, the 2020 regional land use/ land cover map of South Africa of 73 classes was further reclassified into 8 (Forested area, Shrub cover, grass cover, water bodies, bare area, farming area, settlements, and developed area) and extracted for the dominating class. The validation of each discreet unit is based on Le Roux's (2012) approach through visual interpretation and vectorization aided by Système Pour l'Observation de la Terre (SPOT) 5 imagery at a scale of 1:10,000. In this study, Google Earth and 216.96 ha reference scale were used, while the visual interpretation was based on the following assumptions per the dominating SEPA class;

- Class 1 observation represents the non-vulnerable area based on a significant proportion (70%) of the area being relatively covered by vegetation, with stable soil conditions, or with natural landscape attributes (Owolabi *et al.*, 2023).

- Class 2 observation represents the area with a significant proportion (35%) of the terrain exhibiting the potential for soil erosion based on exposure of the subsoils in critical/ vulnerable drainage channels, the non-conservative land use/ land cover features, and track evidence of sheet erosion.

- Class 3 observation represents the area with a significant proportion (35%) of the terrain exhibiting clear evidence of rills, inter-rills, subsoils, and channel erosion.

- Class 4 observation represents the area with a significant proportion of gully developments, extensive rills, inter-rills, and unnatural channel dissections with solid evidence of subsoil crevices.

The four classifications were used with the rationale that class-1, -2, and -3 observations would be replicated by SEPA prediction with non-vulnerable, low, and medium soil erosion potential. At the same time, class-4 is expected to replicate SEPA prediction with high and critically high soil erosion potential. Overall, the observed and predicted classes are tested using confusion matrices. The deductions are corroborated by the Regional Land use/ land

cover features of 2020 provided by the Department of Environmental Affairs of South Africa.

3. Results

3.1. Morphometric Parameters analysis

The drainage density (DD) computation shows that the Tyume River Basin (TRB) is characterized by an elongated but dendritic fluvial network with a southward river flow influenced by terrain physiography (Figure 3A). The high DD are areas of surface water accumulation. Moderate DD areas are active hydraulic actions and soil transportation, while low sections are areas of infrequent drainage activities. The shallow sections are ridges bordering the watershed. Topographic wetness index maps have been noted to provide information on the areas of soil moisture accumulation, soil depth, soil thickness, and zones of possible offsite soil erosion by water (Figure 3B). The classification of the TWI revealed that the high TWI (4%) has the least coverage, followed by the moderate TWI (8%), the low (36%), and the none TWI section (52%) having the largest coverage. Terrain ruggedness index (TRI) reveals landforms corresponding to terrain features such as hilly terrains, ridges, heaps, cols, passes, and valleys (Figure 3C). The high TRI zones correlate visually with the geologic basement, exhibiting high erosion resistance zones. At the same time, the low TRI aligns with the plain and tends to exhibit soil erosion vulnerability. The Topographic position index (TPI) plot impresses with the
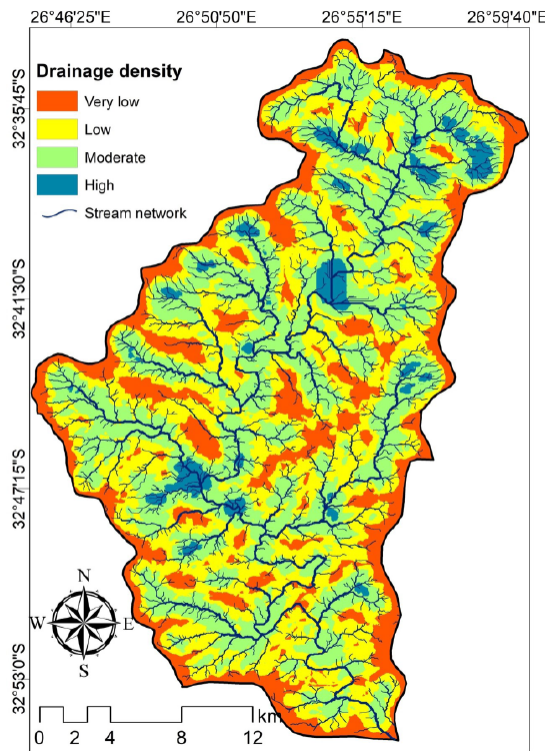

Figure 3A. Drainage density together with the stream network of Tyume basin.

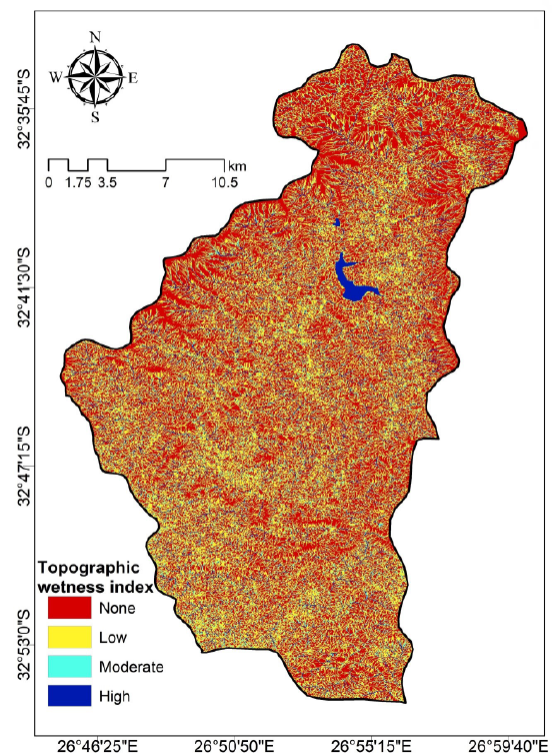*Figura 3A. Densidad de drenaje junto con la red de arroyos de la cuenca de Tyume.*

Figure 3B. Topographic wetness index of Tyume Basin.

Figura 3B. Índice de humedad topográfica de la cuenca de Tyume.
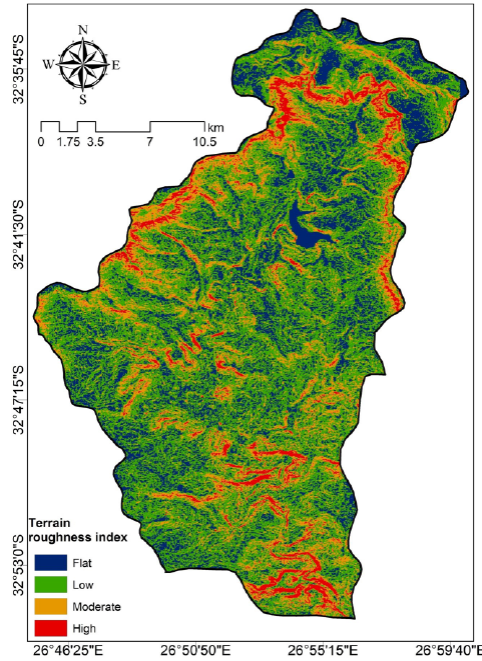
Figure 3C. Terrain roughness index of Tyume Basin.
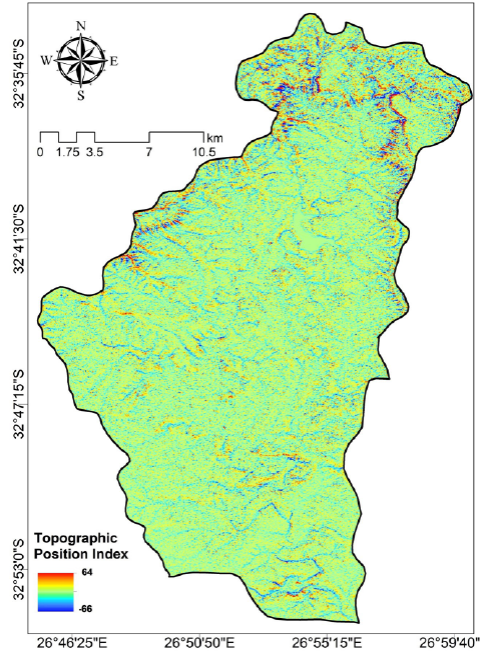*Figura 3C. Índice de rugosidad del terreno de la cuenca de Tyume.*

Figure 3D. Topographic position index of Tyume Basin.
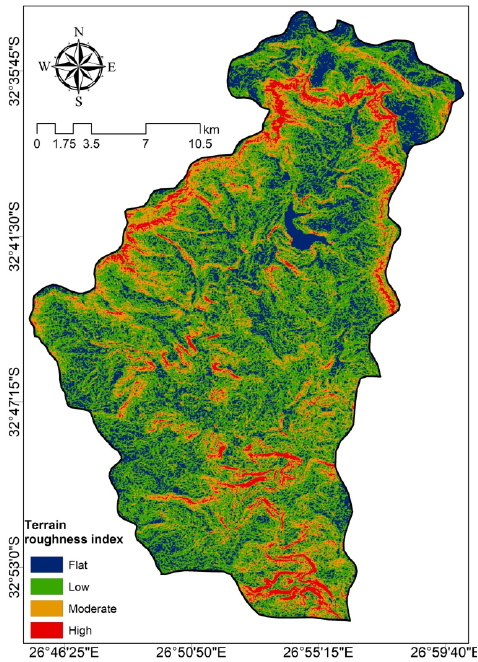*Figura 3D. Índice de posición topográfica de la cuenca de Tyume.*

Figure 3E. Vector roughness measure of Tyume Basin.
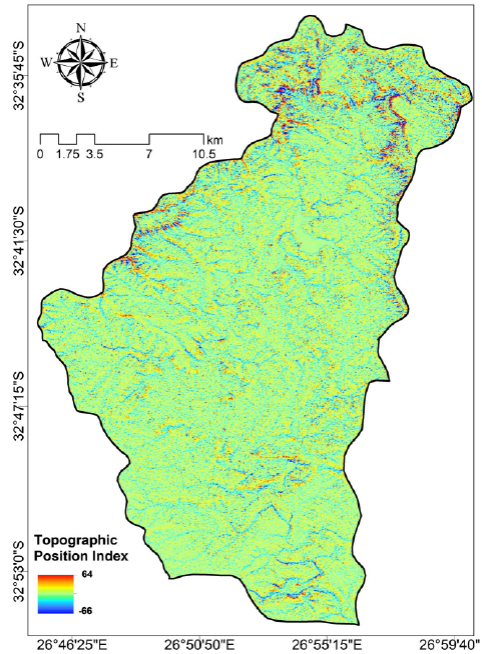*Figura 3E. Medida de rugosidad vectorial de la cuenca de Tyume.*

Figure 3F. Lithology of Tyume basin (Robb *et al.*, 2006).
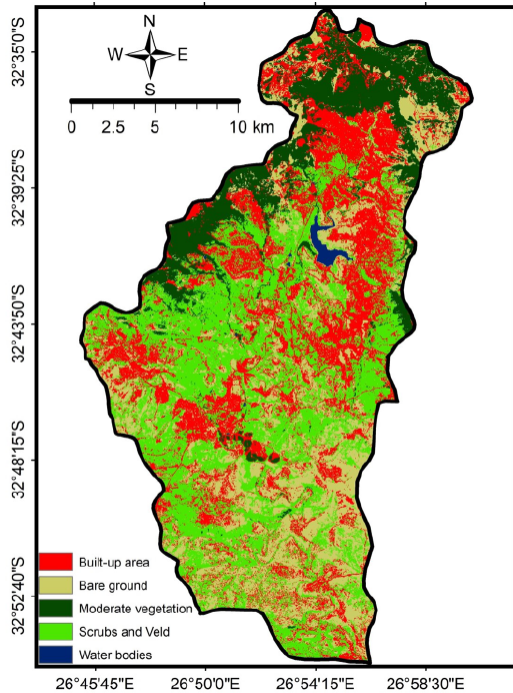*Figura 3F. Litología de la cuenca Tyume (Robb et al., 2006).*

Figure 3G. Land use-cover map of Tyume basin for the year 2019.

Figura 3G. Cobertura de uso del suelo de la cuenca de Tyume para el año 2019.

terrain physiography, thus depicting the depressions along the Tyume River track (Figure 3D). The high TPI are areas of significant concavity, signaling the potential for gully or valley development, while the low TPI are areas of convexity and the possible lines of a continuous slope. The Vector roughness measure (VRM) plot provides information on the area of abrupt curvature based on the integration of slope and aspect variability (Figure 3E). The high VRM captures the areas of high hydraulic pressure and erosivity potential, while the low VRM captures the areas of low curvature and low erosivity potential.

3.2. Gology

The geological information of the Tyume basin comprises the basement (hard rock), the sedimentary rock (soft rock), and the qua-

ternary sediments covering about 553 km^2 (81%), 90 km^2 (13%), and 12.85 km^2 (2%) (Figure 3F). The Quaternary sediments are products of fluvial outwash from bedform assemblages through the complex interplay of climate and geo-allogenic processes such as tectonic subsidence, rifting, and hinterland erosion (Wilson *et al.*, 2014; Owolabi *et al.*, 2021b). The high mudstone content of the Balfour Formation typifies its high tendency for soil erodibility; hence, it scored higher weightage than the Katberg Formation, Middleton Formation, Quaternary sediments, and the Dolerite, which is highly resistant to hydraulic fracturing.

3.3. Land use/ cover

The LU/C map shows that the vegetation covers 48% of the entire TRB, with the forest and scrub-and-veld occupying 89.88 km^2 and 215.25 km^2 (Figure 3G). The water bodies were visible within 3.65 km^2. The built-up area and the bare ground covered 178.66 km^2 and 154.92 km^{2,} respectively (Figure 3G). Vegetation is the most significant LU/C feature to soil erosion mitigation due to its root system and canopy cover actions against erosion due to overland flow, interflow, and rain-splash, as well as the organic deposits improving soil structure against erodibility (Parwada and Van Tol, 2016). Due to the essential role of vegetation, the woodland and scrub-to-veld cover are ranked as the least. The bare is ranked highest due to its high vulnerability to soil erosion. In contrast, the water area is ranked lower than the bare ground because soil detachment and abrasion are highest on the bank. At the same time, transportation and degradation only occur within the water body.

3.4. Vulnerability map of water soil erosion

Soil erosion potential area index obtained ranges in vulnerability from critically high, ap-
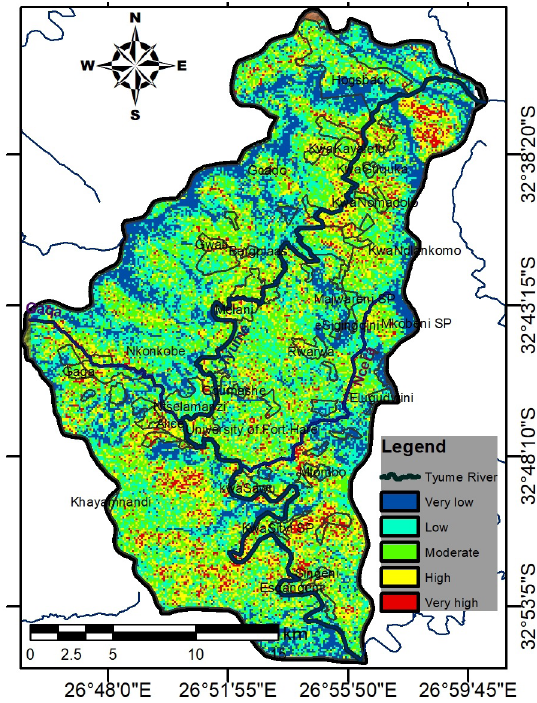
Figure 4. Tyume River basin vulnerability by soil erosion by water showing the vulnerable spots within the basin.

Figura 4. Vulnerabilidad de la cuenca del río Tyume por la erosión hídrica.

Figure 5A. View of areas of mild soil erosion by water (shown with blue arrows).

Figura 5A. Vista de áreas de leve erosión del suelo por el agua (mostradas con flechas azules).

proximately 40 km^2 (6%), high, 135 km^2 (20%), medium, 209 km^2 (31%), and low, 186 km^2 (27%), to a non-vulnerable degree, 113 km^2 (17%) (Figure 4). The zone of high soil erosion vulnerability is concentrated in the northeast and west, where land development is high, and in the southwest and south, where plain and riparian activities favor intense cultivation and pastures. Fundamentally, drainage paths often follow alterable morphogenetic paths with high permeability or susceptibility to hydraulic action. Exposure and lowering of soil aggregate with the drainage path raise channel vulnerability and the development of rills.

3.5. Corroboration of the soil erosion vulnerability map

The sixty-three assessment points were randomly picked from moderate to highly vulnerable zones for Google Earth scenery sampling and analysis. Of the sixty-three points, seven points have no soil erosion indication or erosional drainage, while twenty-one show mild soil erosional tracks, as shown in Figures 5 A – B. About 55% of the sampled field points show distinct erosional features of gully, rill, and sheet erosions and areas where mass wastes resulted from aggregation of the soil erosions (Figure 5B). Related grid codes of sampled points were extracted in the ArcMap to provide a platform for assessing model accuracy, validation, and corroboration (Table 8). The coefficient of determination (R^2) shows a reliable confidence level in the model as the actual field condition is average (Figure 6). This suggests that about 55% percent of the degree of evaluation is satisfied by the assessment and indicates that SEPA approach can be adopted for soil erosion modeling if the statistical classifier and other significant factors can be included. The model was further diagnosed using the Receiver Operating Characteristics curve (ROC) due to its robustness and the in-depth information it provides (Figure 7). The plot indicated that the model
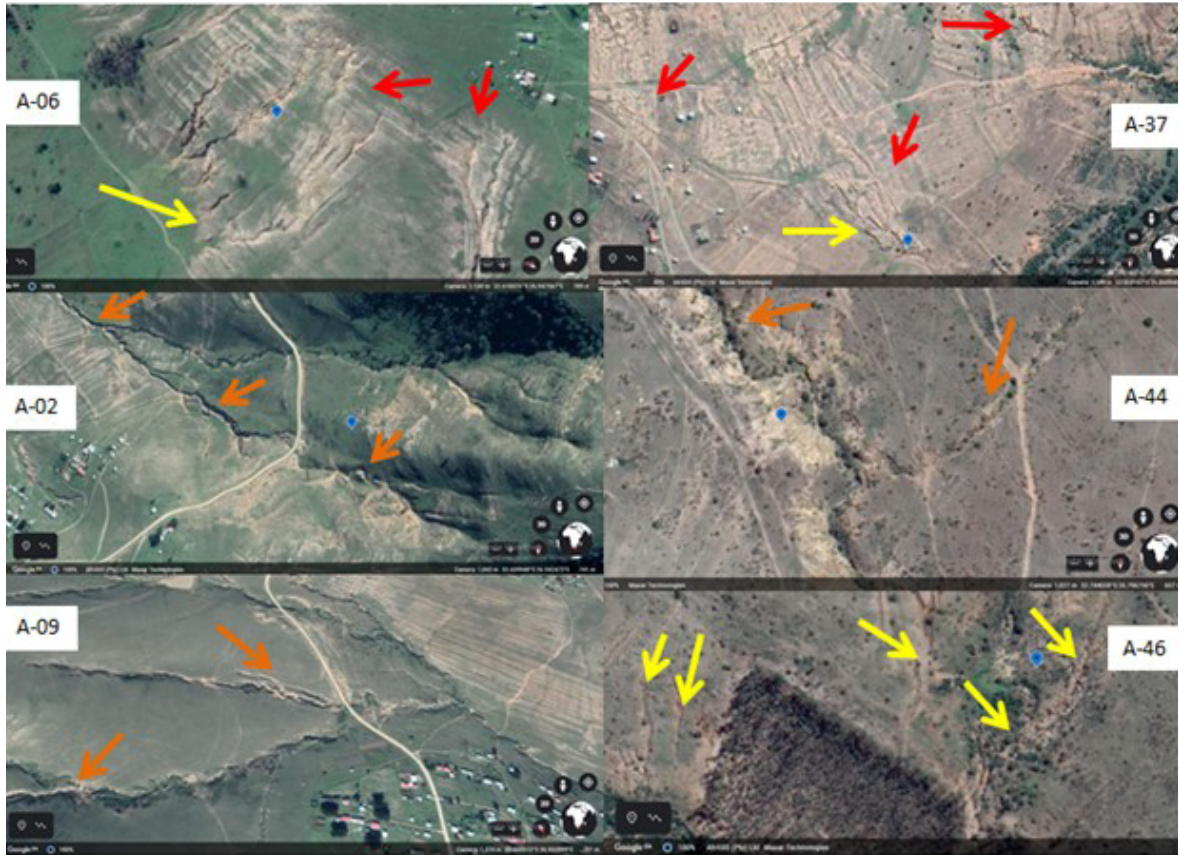
Figure 5B. View of tracks of soil erosion by water (Areas of mass waste resulting from rill erosion are shown with red arrows, rill erosion tracks are shown with yellow/orange arrows)

Figura 5B. Vista de las huellas de la erosión hídrica del suelo (las áreas de depósitos resultantes de la erosión en surcos se muestran con flechas rojas, las huellas de la erosión en surcos se muestran con flechas amarillas/naranjas).

Figure 6. Plot of accuracy assessment of Tyume soil erosion by water modeling.

Figura 6. Gráfico de evaluación de la precisión de la erosión del suelo de Tyume mediante modelado hídrico.

Figure 7. Receiver Operating Characteristics curve of soil erodibility validation.

Figura 7. Curva de características operativas del receptor de validación de la erosionabilidad del suelo.

Table 8. Data of estimated erosion proneness with Tyume River basin
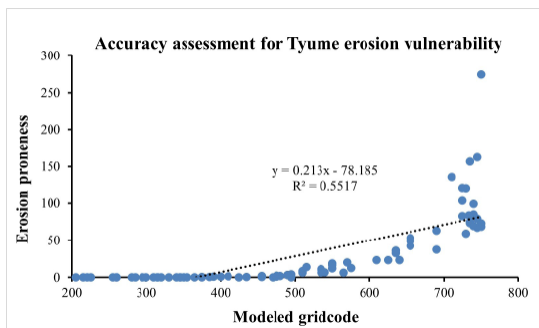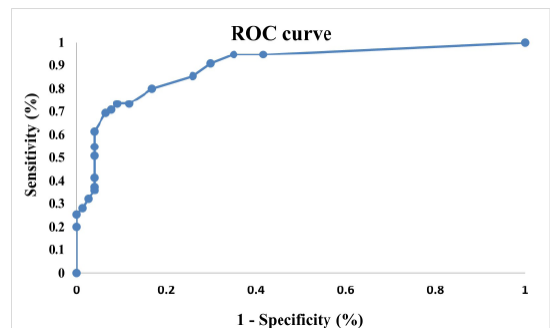
Tabla 8. Ubicación del centroide de la cuenca, tipo de cuenca cuaternaria y área en kilómetros cuadrados.

Longitude (Degree)	Latitude (Degree)	Counts	ID-code	Bareness	Slope	Erodibility km²	Camera km²
26.977	-32.623	730	A-01	4	4	120.676	753
26.977	-32.634	725	A-02	3	4	261.048	759
26.981	-32.613	690	A-03	3	4	37.5937	1035
26.951	-32.626	745	A-04	4	2	78.823	1179
26.936	-32.638	750	A-05	3	2	68.236	1027
26.944	-32.617	745	A-06	4	3	162.453	784
26.951	-32.656	655	A-08	2	3	48.745	1189
26.951	-32.67	750	A-09	3	3	274.65	789
26.931	-32.68	540	A-10	3	1	6.841	1060
26.903	-32.657	495	A-12	1	1	0.231	2160
26.956	-32.736	735	A-13	2	2	74.792	1304
26.94	-32.729	565	A-14	2	1	6.562	1217
26.935	-32.75	425	A-15	1	1	0.113	1843
26.913	-32.767	535	A-16	2	2	11.286	922
26.904	-32.797	740	A-17	3	2	69.474	1130
26.902	-32.8	735	A-18	3	3	73.392	1668
26.911	-32.808	745	A-19	3	2	67.138	1047
26.869	-32.811	730	A-20	4	2	59.261	811
26.87	-32.838	435	A-21	3	1	0.626	1520
26.917	-32.838	635	A-22	2	1	35.927	943
26.901	-32.843	550	A-23	2	2	16.588	2326
26.912	-32.863	740	A-24	3	3	98.763	668
26.931	-32.887	635	A-25	3	2	32.558	864
26.892	-32.877	550	A-26	3	3	12.256	1202
26.853	-32.877	455	A-27	2	1	0.102	2139
26.828	-32.846	490	A-28	1	1	0.145	1048
26.829	-32.864	495	A-29	1	1	0.156	1150
26.816	-32.85	470	A-30	1	1	0.245	1342
26.844	-32.835	475	A-31	3	3	0.287	1334
26.87	-32.825	490	A-32	4	3	0.234	1374
26.901	-32.844	640	A-33	2	2	23.316	867
26.837	-32.818	535	A-34	3	2	10.556	1460
26.831	-32.819	575	A-35	3	2	2.723	1162
26.817	-32.798	455	A-36	2	1	0.532	940
26.823	-32.824	710	A-37	4	3	135.939	865
26.815	-32.791	410	A-38	2	1	0.362	1609
26.826	-32.775	570	A-39	3	1	2.31	1334
26.785	-32.762	750	A-42	4	2	72.661	1204
26.802	-32.746	625	A-43	4	2	23.153	3379

is reliable and will perform well due to the ROC curve's concavity, that is, the proximity of threshold 1 (optimum tangential path of the parabola), which drifts away from the diagonal to the standard angle. The area under the ROC is 0.867, which implies that the degree of separability of the model between the positive and the negative outcome to the actual soil erodibility potential is excellent, reliable, and highly predictive. The optimum sensitivity and sphericity lie on 510 grid-code; hence, a grid-code value more significant than this indicates the possible existence of soil erosion features. The validation shows no discrimination between the gully and rill erosion features captured by the high zones of the vulnerability assessment. This is probably due to the resolution of the digital elevation model used, which was 30 m by 30 m.

Meanwhile, most of the gully features were continuous from the rill features, whereas the latter is the dominant feature in the basin. The erosion features are peculiar to the areas of bareness, which are often near settlements or townships. As guided by Google Earth corroboration, most of the eroded areas within the bare zones were characterized by rill erosion. Areas of high relief and slope also contribute significantly to the soil erosion features where most features taper from sheet to gully erosional features. Most of the erosional features were connected to the natural drainage. The validation exercise shows that many vulnerable spots are associated with either gullies or a collection of long inter-rills. In the north, most of them lie in the bare or grassland area, while in the center and south of the basin, the vulnerable area occupies the cultivated and bare grounds surrounding the riparian lands (Figure 5A; A-10, A-14). The broadest vulnerable south area is characterized by an overgrazed expanse of rangeland whose drainage channel is badly mutilated, possibly by overstocking or uncontrolled cattle patronage.

Similarly, the corroboration based on holistic assessment with GIS fishnet and Google Earth validation is presented in Table 9. The holistic investigation based on the GIS fishnet captured 219 zones per 216.96 ha. The dominating (majority) SEPA attributes which constitute the predicted values comprise 31, 66, 97, and 25 counts for Class-1, -2, -3, and -4, relative to the 53, 93, 61, and 12 counts for the accurate observation based on Google Earth validation, respectively. Also, the matrices of the observed classes and the major SEPA predictions generated the result presented in Table 10. The investigation showed that 38% of areas identified as being dominantly non-vulnerable were contrarily associated with low soil erosion potential, while SEPA predictions are 64%, 49%, and 44% accurate for Class-2, -3, and -4, thus depicting an overestimation of soil erosion potential. The regional LUC showed that the erroneous estimates lie in areas dominated by grassland, partly affected by bareness within the hillslope, followed by the forested areas in the hillslope partly associated with bareness and subsoil exposure. The corroboration showed that the topographic model for soil erosion is excellently sensitive to areas with glaring soil erosion development. At the same time, it provides a considerable approximation for the highly eroded and non-vulnerable area, drawing from the sensitivity and specificity results. The overall accuracy and Kappa coefficient of SEPA prediction are 55% and 36%, respectively, suggesting moderate reliability of the model, although with a low representation of the actual ground situation.

4. Discussion

The modeling of TRB enabled the characterization of the terrain susceptibility to soil erosion into five vulnerable zones: critically high, high, medium, low, and none. The model is computed by integrating the thematic layers of morphometric parameters, LU/C, and

Table 9. Few of the data drawn from the holistic visual evaluation based on Le Roux (2012).
Tabla 9. Algunos de los datos extraídos de la evaluación visual holística basada en Le Roux (2012).

SN	Longitude	Latitude	Predicted	Observed	SN	Longitude	Latitude	Predicted	Observed
1	26.88444	-32.9053	1	1	43	26.92059	-32.8357	4	4
2	26.89649	-32.9053	1	1	44	26.93264	-32.8357	4	4
3	26.90854	-32.9053	2	1	45	26.81214	-32.8183	2	1
4	26.92059	-32.9053	1	2	46	26.82419	-32.8183	3	1
5	26.93264	-32.9053	3	3	47	26.83624	-32.8183	4	3
6	26.86034	-32.8879	2	1	48	26.84829	-32.8183	4	3
7	26.87239	-32.8879	3	2	49	26.86034	-32.8183	3	1
8	26.88444	-32.8879	3	2	50	26.87239	-32.8183	4	4
9	26.89649	-32.8879	2	1	51	26.88444	-32.8183	3	3
10	26.90854	-32.8879	2	2	52	26.89649	-32.8183	2	2
11	26.92059	-32.8879	2	2	53	26.90854	-32.8183	3	3
12	26.93264	-32.8879	4	4	54	26.92059	-32.8183	3	3
13	26.82419	-32.8705	3	2	55	26.80009	-32.8009	3	2
14	26.83624	-32.8705	4	3	56	26.81214	-32.8009	3	2
15	26.84829	-32.8705	4	3	57	26.82419	-32.8009	3	1
16	26.86034	-32.8705	4	3	58	26.83624	-32.8009	1	1
17	26.87239	-32.8705	4	3	59	26.84829	-32.8009	2	2
18	26.88444	-32.8705	3	2	60	26.86034	-32.8009	3	2
19	26.89649	-32.8705	3	3	61	26.87239	-32.8009	3	1
20	26.90854	-32.8705	3	3	62	26.88444	-32.8009	3	1
21	26.92059	-32.8705	3	3	63	26.89649	-32.8009	3	3
22	26.93264	-32.8705	2	2	64	26.90854	-32.8009	4	4
23	26.81214	-32.8531	3	1	65	26.92059	-32.8009	1	2
24	26.82419	-32.8531	3	1	66	26.93264	-32.8009	1	2
25	26.83624	-32.8531	3	1	67	26.77599	-32.7835	4	3
26	26.84829	-32.8531	4	2	68	26.78804	-32.7835	2	2
27	26.86034	-32.8531	3	2	69	26.80009	-32.7835	1	2
28	26.87239	-32.8531	4	3	70	26.81214	-32.7835	3	2
29	26.88444	-32.8531	3	2	71	26.82419	-32.7835	4	4
30	26.89649	-32.8531	2	2	72	26.83624	-32.7835	4	3
31	26.90854	-32.8531	4	2	73	26.84829	-32.7835	2	2
32	26.92059	-32.8531	3	3	74	26.86034	-32.7835	3	2
33	26.93264	-32.8531	4	2	75	26.87239	-32.7835	2	2
34	26.81214	-32.8357	3	1	76	26.88444	-32.7835	3	3
35	26.82419	-32.8357	3	1	77	26.89649	-32.7835	3	2
36	26.83624	-32.8357	3	1	78	26.90854	-32.7835	2	1
37	26.84829	-32.8357	3	2	79	26.92059	-32.7835	2	2
38	26.86034	-32.8357	2	1	80	26.93264	-32.7835	2	2
39	26.87239	-32.8357	2	2	81	26.77599	-32.7661	3	2
40	26.88444	-32.8357	3	2	82	26.78804	-32.7661	3	2
41	26.89649	-32.8357	2	2	83	26.80009	-32.7661	3	3
42	26.90854	-32.8357	4	3	84	26.81214	-32.7661	1	2

geology. The deduction of the ROC curves, 89.9%, validates the vital essence of the geomorphic-based model for the soil erosion susceptibility model. At the same time, the confusion matrices clarify the model's performance in terms of its sensitivity, specificity, accuracy, extent of representation, excesses, and limitations. At the same time, it corroborates ROC curve finding. Based on the holistic corroboration with confusion matrices (Tables 9-10), the exceptionally high and high, accentuated by class-4 (44%), corresponded with the Hillslope farming area possibly abandoned or used for farm-

ing. Some are associated with bareness and deciphered to have served as a farming area before being abandoned. There are cases where urbanization induces channel erosion. The regional land use/cover map confirmed that grasses covered most of this area, whereas Google Earth showed traces of fallowing and abandonment.

The erroneously captured area was dominated by scanty shrub covered with exposed subsoil. The moderately eroded portion, accentuated by Class-3 dominance, is mainly associated with bareness and channel ero-

Table 10. Confusion matrices for the holistic evaluation of model performance.
Tabla 10. Matrices de confusión para la evaluación general de la aplicación del modelo.

Observed Google Earth classification value

		Class-1	*Class-2*	*Class-3*	*Class-4*
SEPA Predicted Value	*Class-1*	19	12	0	0
	Class-2	22	42	2	0
	Class-3	12	36	48	1
	Class-4	0	3	11	11

	Class: 1	*Class: 2*	*Class: 3*	*Class: 4*
Sensitivity	0.358	0.452	0.787	0.917
Specificity	0.928	0.810	0.690	0.932
Pos Pred Value	0.613	0.636	0.495	0.440
Neg Pred Value	0.819	0.667	0.893	0.995
Prevalence	0.242	0.425	0.279	0.055
Detection Rate	0.087	0.192	0.219	0.050
Detection Prevalence	0.142	0.301	0.443	0.114
Balanced Accuracy	0.643	0.631	0.738	0.925

Overall Statistics

Accuracy: 0.5479
95% CI: (0.4795, 0.6151)
No Information Rate: 0.4247
P-Value [Acc > NIR]: 0.0001602
Kappa: 0.3616
Mcnemar's Test P-Value: < 0.00000

sion. The soil type also played a significant role in the erodibility of the soil, as shown by the numerous subsoil exposures in the area. With TRB being dominated by Calcic Vertisol and Calcaric Regosol (Dijkshoorn *et al.*, 2008), an uncoordinated use of such land, such as excessive grazing, hillslope farming, and uncoordinated afforestation after fallowing may render Vertisol and Regosol soil types vulnerable to soil erosion. Basga *et al.* (2020) noted that vertisols and regosols are highly susceptible to soil erosion by water due to their expansivity and slow filtration. Both soils dominate areas where farming activities and land abandonment possibly render the terrain vulnerable to soil erosion. Numerous authors, including van Leeuwen *et al.* (2019), Yue *et al.* (2020), and Shtober-Zisu *et al.* (2024), highlighted several cases of soil degradation process initiated by farmland abandonment as posited in this study. However, the significant factor captured as the driver of soil erosion is the sparsely vegetated, fallow, or bare surface with weak topsoil, where settlement, farming activities, or farm abandonment are evident, especially by the hillslope and frequently drained area (Figure 4).

The spatial trend exhibited by the soil erosion vulnerability map indicated the concentration of extreme soil erosion vulnerability in the northwest, west, southwest, and south. The northeast represents the high relief area with abrupt concavity and slope, which may enhance runoff-erosivity by the hillslope and create an erosive plunge at the foothill. High relief area in Tyume Catchment to the east has been classified as the hinterland of the Great Escarpment, where upsurging tectonically emplacement sub-mountain range could trigger orographic rainfall with high intensity and erosivity (Zengeni *et al.*, 2016). As a result, the terrain analysis provides vital information about the soil erosion vulnerable areas as induced by the topographic features. Being aided by LUC and the geology map, the MPs

suitably fulfill the geomorphic and hydrologic requirements of soil erosion models by simulating the areas of possible runoff erosivity based on the terrain roughness, concavity, and topographic position closeness based on the TRI, VRM, and TPI deduction. The DD and TWI also indicate the area of frequent runoff, accumulation, and channel erosivity. Shtober-Zisu *et al.* (2024) remarked on the excellent performance of TRI in identifying areas with soil erosion incision due to high rainfall erosivity.

Meanwhile, Owolabi *et al.* (2020) provided the vast application of DD and TWI for determining the area of hydrologic inundation, resulting in the dissolution and degradation of the vulnerable regions induced by land use/cover activities based on the underlying geologic type. Based on the extreme soil erosion vulnerability in the northeast, this study shared common ground with Hembram *et al.* (2019), who noted that soil erosion showed the highest sensitivity to relief characteristics among other contributing morphometric factors. Prior investigations also demonstrated the alarming rate of soil erosion in the high reliefs within the Eastern Cape with similar LU/C patterns and soil types (Phinzi and Ngetar, 2019; Libala *et al.*, 2020; Gwapedza *et al.*, 2021).

The west, southwest, and south of Tyume are relatively flat and low in altitude; however, severe bareness is connected with the built-up area. Tyume South is characterized by a high rate of rural settlement, whose leading economy is dominated by livestock and traditional farming (Fatumo *et al.*, 2021). Chungag *et al.* (2017) noted that Tyume south is characterized by free-range animal husbandry and disturbance of the drainage channel, and physical disaggregation of soil cover and clods contributes significantly to soil erosion vulnerability. Boardman *et al.* (2017) asserted that the current land degradation, which cul-

minates in badlands and gullies, developed from the 200 years of history of overgrazing. Hebinck *et al.* (2018) noted that the Tyume basin has been subject to unguarded continuous communal grazing, which the cattle herders committee politically strengthened from 1847 to 2005. Hence, the bareness and topsoil disturbance rendering the hilly terrain vulnerable to soil erosion is possibly due to the poorly coordinated farm practice and cropland abandonment (Sibiya *et al.*, 2023). The study seeks advocacy for the remediation of sites already degraded by unguarded LU/C activities through afforestation policy, considering the negative response of degraded land to the natural hydrological process and the potential for soil erosion.

The soil erosion vulnerability findings strongly correspond to Mhangara *et al.*'s (2012) findings on soil loss within the Tyume section of the Keiskamma catchment, based on the Sediment Assessment Tool for Effective Erosion Control approach. This study agrees with Mhangara *et al.* (2012) deduction that vegetation enrichment is highly instrumental in soil erosion mitigation. However, Mhangara *et al.* (2012) produced a significant error matrix consistent with the conservation rating factor used. Therefore, this study shows that geology information and terrain ruggedness index are better hybrids than the conservation rating factor used in Mhangara *et al.* (2012) approach, as the error matrix within the extremely rugged area was significantly reduced.

Specifically, this study highlighted the problem of unsustainable land management in the Tyume Basin, which is not strictly driven by nature. Therefore, this study calls on the Department of Environment, Forestry and Fisheries, Department of Water and Sanitation, and other concerned stakeholders to review the policy against human encroachment on the riparian lands and the mutilation of river channels.

5. Conclusions

An integrated framework of soil erosion assessment based on clustering of geo-morphic parameters with land use/ land cover and geology theme has depicted the substantial role of morphometric parameters in the qualitative assessment of soil erosion in areas with topographic complexities. The novelty of the work lies in the selection of GIS-based physiographic themes in achieving a site-specific soil erosion modeling. The following inferences can be drawn from the study:

- The morphometric-based soil erosion model proved reliable in the absence of pluviometric and pedometric data.

- The model provides a qualitative inference of the hotspots and cold-spots of soil erosion vulnerability.

- The study highlights human encroachment, terrain bareness, hillslope farming, and land abandonment as the cogent factors driving soil erosion in the terrain.

- Appositional evaluation of the fluvial network orientation, the topographic position index information, and the land use/ land cover deduction provides substantial information on the vulnerability of the riparian environment in the southern section of the Tyume.

Due to resource constraints, a significant limitation in this study is the inability to embark on a field sampling for periodic rainfall data gathering and soil physicochemical properties to corroborate the findings with a spatial distribution map of rainfall erosivity and soil erodibility. However, this is recommended for future research, mainly to undertake a scenario mapping of an improved revised universal soil loss equation with some of the validated morphometric parameters presented in this study. Overall, the present approach is suita-

ble for qualitative soil erosion assessment in a topographically complex environment.

Acknowledgements

Compliance with ethical standards

This work is entirely a desktop study with a reconnaissance survey for ground-truthing, and therefore, no animal or human participant was involved in the research.

Conflict of interest

The authors declare that there is no conflict of interest.

References

Aloui, S., Mazzoni, A., Elomri, A., Aouissi, J., Boufekane, A., Zghibi, A. (2023). A review of Soil and Water Assessment Tool (SWAT) studies of Mediterranean catchments: Applications, feasibility, and future directions. *Journal of Environmental Management*, 326, 116799. https://doi.org/10.1016/j.jenvman.2022.116799

Amatulli, G., McInerney, D., Sethi, T., Strobl, P., Domisch, S. (2020). Geomorpho90m, empirical evaluation and accuracy assessment of global high-resolution geomorphometric layers. *Scientific Data*, 7(1), 1-18. https://doi.org/10.1038/s41597-020-0479-6

Arnold, J.G., Srinivasan, R., Muttiah, R.S., Williams, J.R. (1998). Large area hydrologic modeling and assessment part I: model development 1. *Journal of the American Water Resources Association*, 34(1), 73-89. https://doi.org/10.1111/j.1752-1688.1998.tb05961.x

Arumugam, T., Kinattinkara, S., Velusamy, S., Shanmugamoorthy, M., Murugan, S. (2023). GIS

based landslide susceptibility mapping and assessment using weighted overlay method in Wayanad: A part of Western Ghats, Kerala. *Urban Climate*, 49, 101508. https://doi.org/10.1016/j.uclim.2023.101508

Avand, M., Kuriqi, A., Khazaei, M., Ghorbanzadeh, O. (2022). DEM resolution effects on machine learning performance for flood probability mapping. *Journal of Hydro-Environment Research*, 40, 1-16. https://doi.org/10.1016/j.jher.2021.10.002

Basga, S.D., Temga, J.P., Tsozué, D., Gove, A., Sali, B., Nguetnkam, J.P. (2020). Erodibility of Vertisols in relation to agricultural practices along a toposequence in the Logone floodplain. *Soil & environment*, 39(1), 1-12. https://doi.org/10.25252/SE/2020/101855

Basson, G., Bosman, E., Vonkeman, J. (2022). Reservoir sedimentation mitigation measures to deal with a severe drought at Graaff-Reinet, South Africa. In *E3S Web of Conferences* (Vol. 346, p. 03012). EDP Sciences. https://doi.org/10.1051/e3sconf/202234603012

Bhatt, S., Ahmed, S.A. (2014). Morphometric analysis to determine floods in the Upper Krishna basin using Cartosat DEM. *Geocarto Imnternational*, 29(8), 878-894. https://doi.org/10.1080/10106049.2013.868042

Biswa, J., Giri, B. (2023). RUSLE and AHP based soil erosion risk mapping for Jalpaiguri district of West Bengal, India. *Proceedings of the Indian National Science Academy*, 89(4), 869-883. https://doi.org/10.1007/s43538-023-00197-3

Boardman, J., Foster, I.D., Rowntree, K.M., Favis-Mortlock, D.T., Mol, L., Suich, H., Gaynor, D. (2017). Long-term studies of land degradation in the Sneeuberg uplands, eastern Karoo, South Africa: a synthesis. *Geomorphology*, 285, 106-120. https://doi.org/10.1016/j.geomorph.2017.01.024

Busico, G., Grilli, E., Carvalho, S.C., Mastrocicco, M., Castaldi, S. (2023). Assessing Soil Erosion Susceptibility for Past and Future Scenarios in Semiarid Mediterranean Agroecosystems. *Sustainability*, 15(17), 12992. https://doi.org/10.3390/su151712992

Butler, K., 2013. Band combination for Landsat 8. Imagery & Remote sensing. https://www.esri.com/arcgis-blog/products/product/imagery/band-combinations-for-landsat-8/

Cassidy, R., Doody, D.G., Watson, C.J. (2017). Impact of legacy soil phosphorus on losses in drainage and overland flow from grazed grassland soils. *Science of the Total Environment*, 575, 474-484. https://doi.org/10.1016/j.scitotenv.2016.07.063

Chungag, A., van Tol, J.J., Magagula, B. (2017). Effect of unguided cattle husbandry on selected soil physical properties in common property regimes in Alice, Eastern Cape Province, South Africa. *Range Management and Agroforestry*, 38(2), 176-180.

Deribew, K.T., Arega, E., Moisa, M.B. (2024). Prediction of the topo-hydrologic effects of soil loss using morphometric analysis in the upper Bilate watershed. *Bulletin of Engineering Geology and the Environment*, 83(5), 162. https://doi.org/10.1007/s10064-024-03634-9

Dimple, Singh, P.K., Kothari, M., Yadav, K.K., Bhakar, S.R. (2023). Multi-criteria decision analysis for groundwater potential zones delineation using geospatial tools and Analytical Hierarchy Process (AHP) in Nand Samand Catchment, Rajasthan, India. *Environment, Development and Sustainability*, 1-35. https://doi.org/10.1007/s10668-023-03177-1

Dijkshoorn, J.A., van Engelen, V.W.P., Huting, J.R.M.l. (2008). *Soil and landform properties for LADA partner countries (Argentina, China, Cuba, Senegal and The Gambia, South Africa, and Tunisia)*. ISRIC report 2008/06 and GLADA report 2008/03, ISRIC – World Soil Information and FAO, Wageningen (23).

Dutta, A., Ray, R., Banerjee, M. (2024). Multi-criteria-based decision making approach for soil erosion susceptibility modelling of Sali River Basin, Bankura, India. *Environment, Development and Sustainability,* 1-26. https://doi.org/10.1007/s10668-024-04736-w

Dwivedi, R.S. Ramana, K.V. (2003). The delineation of reclamative groups of ravines in the Indo-Gangetic alluvial plains using IRS-1D LISS-III data. *International Journal of Remote Sensing*, 24(22), 4347-4355. https://doi.org/10.1080/0143116031000116994

Department of Water and Sanitation (DWS) (2017). *Hydrological services - surface water: Reservoir sites*, https://www.dwa.gov.za/Hydrology/Verified/HyCatalogue.aspx..

Farhan, Y. Nawaiseh, S. (2015). Spatial assessment of soil erosion risk using RUSLE and GIS techniques. *Environmental Earth Sciences*, 74(6), 4649-4669. https://doi.org/10.1007/s12665-015-4430-7

Fatumo, D.E., Ngwenya, S., Shibeshi, Z., Aduradola, O.J., Azeez, A.N. (2021). Impact of Information and Communication Technology in Enhancing Food Security in a Rural Area: Alice Community as a Case Study. In *2021 IST-Africa Conference (IST-Africa)* (pp. 1-8). IEEE.

Flanagan, D.C. Nearing, M.A. (1995). *USDA-Water erosion prediction project: Hillslope profile and watershed model documentation. National Soil Erosion Research Laboratory, West Lafayette, Indiana*, Report No. 10., 12.3 https://www.ars.usda.gov/ARSUserFiles/ (accessed 12 October 2020).

Ghosh, P., Lepcha, K. (2019). Weighted linear combination method versus grid based overlay operation method–A study for potential soil erosion susceptibility analysis of Malda district (West Bengal) in India. *The Egyptian Journal of Remote Sensing and Space Science*, 22(1), 95-115. https://doi.org/10.1016/j.ejrs.2018.07.002

Gwapedza, D., Nyamela, N., Hughes, D.A., Slaughter, A.R., Mantel, S.K., van der Waal, B. (2021). Prediction of sediment yield of the Inxu River catchment (South Africa) using the MUSLE. *International Soil and Water Conservation Research*, 9(1), 37-48. https://doi.org/10.1016/j.iswcr.2020.10.003

Halder, S., Roy, M.B., Roy, P.K. (2021). Modelling soil erosion risk of a tropical plateau basin to identify priority areas for conservation. *Environmental Earth Sciences,* 80(18), 646. https://doi.org/10.1007/s12665-021-09941-8

Haokip, P., Khan, M.A., Choudhari, P., Kulimushi, L.C., Qaraev, I. (2022). Identification of erosion-prone areas using morphometric parameters, land use land cover and multi-criteria decision-making method: geo-informatics approach. *Environment, Development and Sustainability*, 24(1), 527-557. https://doi.org/10.1007/s10668-021-01452-7

Hasanuzzaman, M., Mandal, M.H., Hasnine, M., Shit, P.K. (2022). Groundwater potential mapping using multi-criteria decision, bivariate statistic and machine learning algorithms:

evidence from Chota Nagpur Plateau, India. *Applied Water Science*, 12(4), 58. https://doi.org/10.1007/s13201-022-01584-9

He, X., Miao, Z., Wang, Y., Yang, L., Zhang, Z. (2024). Response of soil erosion to climate change and vegetation restoration in the Ganjiang River Basin, China. *Ecological Indicators*, 158, 111429. https://doi.org/10.1016/j.ecolind.2023.111429

Hebinck, P., Mtati, N., Shackleton, C. (2018). More than just fields: Reframing deagrarianisation in landscapes and livelihoods. *Journal of Rural Studies*, 61, 323-334. https://doi.org/10.1016/j.jrurstud.2018.01.004

Helmi, A.M. (2023). Quantifying catchments sediment release in arid regions using GIS-based Universal soil loss equation (USLE). *Ain Shams Engineering Journal*, 14(8), 102038. https://doi.org/10.1016/j.asej.2022.102038

Hembram, T.K., Paul, G.C., Saha, S. (2019). Comparative analysis between morphometry and geo-environmental factor-based soil erosion risk assessment using the weight of evidence model: a study on Jainti River Basin, Eastern India. *Environmental Processes*, 6(4), 883-913. https://doi.org/10.1007/s40710-019-00388-5

Hladky, J., Kynický, J., Dvořáčková, H., Elbl, J., Brtnický, M. (2017). Effect of long-term erosion on humus content and quality on chernozem soils. *International Multidisciplinary Scientific GeoConference*: *SGEM*, 17, 179-184. https://doi.org/10.5593/sgem2017/32/S13.024

Hojati, M., Mokarram, M. (2016). Determination of a topographic wetness index using high resolution digital elevation models. *European Journal of Geography*, 7(4), 41-52.

Jadidoleslam, N., Mantilla, R., Krajewski, W.F., Goska, R. (2019). Investigating the role of antecedent SMAP satellite soil moisture, radar rainfall and MODIS vegetation on runoff production in an agricultural region. *Journal of Hydrology*, 579, 124-130. https://doi.org/10.1016/j.jhydrol.2019.124210

Jenness, J. (2006) *Topographic Position Index: An Arc View 3.x tool for analyzing the shape of the landscape*. http://www.jennessent.com/arcview/TPI_jen_poster.htm (Retrieved in 2021-08-26).

Kirkby, M.J. Statham, I. (1975). Surface stone movement and scree formation. *The Journal of Geology*, 83(3), 349-362. https://doi.org/10.1086/628097

Le Roux, J.J. (2012). Gully location mapping at a national scale for South Africa. *South African Geographical Journal= Suid-Afrikaanse Geografiese Tydskrif*, 94(2), 208-218. https://doi.org/10.1080/03736245.2012.742786

Libala, N., Palmer, C.G., Odume, O.N. (2020). Using a trait-based approach for assessing the vulnerability and resilience of hillslope seep wetland vegetation cover to disturbances in the Tsitsa River catchment, Eastern Cape, South Africa. *Ecology and Evolution*, 10(1), 277-291. https://doi.org/10.1002/ece3.5893

Martínez-Murillo, J.F., López-Vicente, M., Poesen, J., Ruiz-Sinoga, J.D. (2011). Modelling the effects of land use changes on runoff and soil erosion in two Mediterranean catchments with active gullies (South of Spain). *Landform Analysis,* 17, 99-104.

Mhangara, P., Kakembo, V., Lim, K.J. (2012). Soil erosion risk assessment of the Keiskamma catchment, South Africa using GIS and remote sensing. *Environmental Earth Sciences*, 65(7), 2087-2102. https://doi.org/10.1007/s12665-011-1190-x

Morgan, R.P.C., Quinton, J.N., Smith, R.E., Govers, G., Poesen, J.W.A., Auerswald, K., Chisci, G., Torri, D., Styczen, M.E. (1998). The European soil erosion model (EUROSEM): a dynamic approach for predicting sediment transport from fields and small catchments. *Earth Surface Processes and Landforms*, 23(6), 527-544. https://doi.org/10.1002/(SICI)1096-9837(199806)23:6<527::AID-ESP868>3.0.CO;2-5

Owolabi, S.T., Madi, K., Kalumba, A.M., Orimoloye, I.R. (2020). A groundwater potential zone mapping approach for semi-arid environments using remote sensing (RS), geographic information system (GIS), and analytical hierarchical process (AHP) techniques: a case study of Buffalo catchment, Eastern Cape, South Africa. *Arabian Journal of Geosciences*, 13, 1-17. https://doi.org/10.1007/s12517-020-06166-0

Owolabi, S.T., Madi, K., Kalumba, A.M. (2021a). Comparative evaluation of spatio-temporal attributes of precipitation and streamflow in Buffalo and Tyume Catchments, Eastern Cape, South Africa. *Environment, Development and*

Sustainability, 23, 4236–4251. https://doi.org/10.1007/s10668-020-00769-z

Owolabi, S.T., Madi, K., Kalumba, A.M., Baiyegunhi, C. (2021b). A geomagnetic analysis for lineament detection and lithologic characterization impacting groundwater prospecting; a case study of Buffalo catchment, Eastern Cape, South Africa. *Groundwater for Sustainable Development*, 12, 100531. https://doi.org/10.1016/j.gsd.2020.100531

Owolabi, S.T., Belle, J.A., Mazinyo, S. (2022). Quantifying intra-catchment streamflow processes and response to climate change within a climatic transitional zone: a case study of Buffalo catchment, Eastern Cape, *South Africa. Mathematics*, 10(16), 3003. https://doi.org/10.3390/math10163003

Owolabi, S.T. Belle, J.A. (2023). Investigating extreme hydrological risk impact on water quality; evidence from Buffalo catchment headwater, Eastern Cape, South Africa. *Environmental Science and Pollution Research*, 1-26. https://doi.org/10.1007/s11356-023-27048-4

Pal, S. (2016). Identification of soil erosion vulnerable areas in Chandrabhaga river basin: a multi-criteria decision approach. *Modelling Earth Systems and Environment*, 2, 1-11. https://doi.org/10.1007/s40808-015-0052-z

Parwada, C., Van Tol, J. (2016). The nature of soil erosion and possible conservation strategies in Ntabelanga area, Eastern Cape Province. *Acta Agriculturae Scandinavica - Section B Soil and Plant Science*, 66(6), 544-552. https://doi.org/10.1080/09064710.2016.1188979

Phinzi, K. Ngetar, N.S. (2019). Land use/land cover dynamics and soil erosion in the Umzintlava catchment (T32E), Eastern Cape, South Africa. *Philosophical Transactions of the Royal Society*, 74(3), 223-237. https://doi.org/10.1080/0035919X.2019.1634652

Pimentel, D. (2010). Corn and cellulosic ethanol problems and soil erosion. Soil quality and biofuel production, In R Lal and B. A. Stewart (Eds). *Soil quality and biofuel production*, CRC Press, Boca Raton, 119–135.

Rahman, M.R., Shi, Z.H., Chongfa, C. (2009). Soil erosion hazard evaluation—an integrated use of remote sensing, GIS, and statistical approaches with biophysical parameters towards management strategies. *Ecological Modelling*, 220(13-14), 1724-1734. https://doi.org/10.1016/j.ecolmodel.2009.04.004

Renard, K.G., Foster, G.R., Weesies, G.A., Porter, J.P. (1991). RUSLE: Revised universal soil loss equation. *Journal of Soils and Water Conservation*, 46(1), 30-33.

Riley, S.J., DeGloria, S.D., Elliot, R. (1999). Index that quantifies topographic heterogeneity. *Intermountain Journal of Sciences*, 5(1-4), 23-27.

Robb, L.J., Brandl, G., Anhaeusser, C.R., Poujol, M., Johnson, M.R., Thomas, R.J. (2006). Archaean granitoid intrusions. *South African Journal of Geology*, 57-94.

Różycka, M., Migoń, P., Michniewicz, A. (2017). Topographic wetness index and terrain ruggedness index in geomorphic characterization of landslide terrains, on examples from the Sudetes, SW Poland. *Zeitschrift für geomorphologie*, Supplementary Issue, 61(2), 61-80. https://doi.org/10.1127/zfg_suppl/2016/0328

Sappington, J.M., Longshore, K.M., Thompson, D.B. (2007). Quantifying landscape ruggedness for animal habitat analysis: a case study using bighorn sheep in the Mojave Desert. *The Journal of Wildlife Management*, 71(5), 1419-1426. https://doi.org/10.2193/2005-723

Sarkar, S., Kanungo, D.P. (2004). An integrated approach for landslide susceptibility mapping using remote sensing and GIS. *Photogrammetric Engineering and Remote Sensing*, 70(5), 617-625. https://doi.org/10.14358/PERS.70.5.617

Schillaci, C., Jones, A., Vieira, D., Munafò, M., Montanarella, L. (2023). Evaluation of the United Nations Sustainable Development Goal 15.3. 1 indicator of land degradation in the European Union. *Land Degradation Development*, 34(1), 250-268. https://doi.org/10.1002/ldr.4457

Sharma, A. (2010). Integrating terrain and vegetation indices for identifying potential soil erosion risk area. *Geospatial Information Science*, 13(3), pp.201-209. https://doi.org/10.1007/s11806-010-0342-6

Shen, H., Zhenga, F., Wen, L., Han, Y., Hu, W. (2016). Impacts of rainfall intensity and slope gradient on rill erosion processes at loessial hillslope. *Soil and Tillage Research*, 155, 429-436. https://doi.org/10.1016/j.still.2015.09.011

Shtober-Zisu, N., Brook, A., Zissu, B. (2024). Soil denudation in the northwestern Negev (Israel) following the Late Byzantine–Early Islamic period. *Geomorphology*, 446, 108983. https://doi.org/10.1016/j.geomorph.2023.108983

Sibiya, S., Clifford-Holmes, J.K., Gambiza, J. (2023). Drivers of Degradation of Croplands and Abandoned Lands: A Case Study of Macubeni Communal Land in the Eastern Cape, South Africa. *Land*, 12(3), 606. https://doi.org/10.3390/land12030606

Smith, M.W. (2014). Roughness in the earth sciences. *Earth-Science Reviews*, 136, 202-225. https://doi.org/10.1016/j.earscirev.2014.05.016

Smith, P., Calvin, K., Nkem, J., Campbell, D., Cherubini, F., Grassi, G., Korotkov, V., Le Hoang, A., Lwasa, S., McElwee, P., Nkonya, E. (2020). Which practices co-deliver food security, climate change mitigation and adaptation, and combat land degradation and desertification? *Global Change Biology*, 26(3), 1532-1575. https://doi.org/10.1111/gcb.14878

Strahler, A.N. (1957). Quantitative analysis of watershed geomorphology. *Eos, Transactions American Geophysical Union*, 38(6), 913-920. https://doi.org/10.1029/TR038i006p00913

Streiner, D.L., Cairney, J. (2007). What's under the ROC? An introduction to receiver operating characteristics curves. *Canadian Journal of Psychiatry,* 52(2), 121-128. https://doi.org/10.1177/070674370705200210

Ugwu, I.E., Emmanuel, K., Vintus, O. (2024). Evaluating the Impacts of Soil Erosion on Selected Hillslopes in UNN Using WEPP Model. *UNIZIK Journal of Engineering and Applied Sciences*, 3(1), 567-572.

van Leeuwen, C.C., Cammeraat, E.L., de Vente, J., Boix-Fayos, C. (2019). The evolution of soil conservation policies targeting land abandonment and soil erosion in Spain: A review. *Land Use Policy*, 83, 174-186. https://doi.org/10.1016/j.landusepol.2019.01.018

Verbakel, J.Y., Steyerberg, E.W., Uno, H., De Cock, B., Wynants, L., Collins, G.S., Van Calster, B. (2020). ROC curves for clinical prediction models part 1. ROC plots showed no added value above the AUC when evaluating the performance of clinical prediction models. *Journal of Clinical Epidemiology,* 126, 207-216. https://doi.org/10.1016/j.jclinepi.2020.01.028

Vieira, A., Oyguc, R. (2024, eds.). *Current Perspectives on Applied Geomorphology*. BoD – Books on Demand, London, 112 p. https://doi.org/10.5772/intechopen.100708

Vrieling, A., Sterk, G., Vigiak, O. (2006). Spatial evaluation of soil erosion risk in the West Usambara Mountains, Tanzania. *Land Degradation Development*, 17(3), 301-319. https://doi.org/10.1002/ldr.711

Weiss, A. (2001). Topographic position and landforms analysis. In Poster presentation, *ESRI user conference*, San Diego, CA (Vol. 200).

Wilson, A., Flint, S., Payenberg, T., Tohver, E., Lanci, L. 2014. Architectural styles and sedimentology of the fluvial lower Beaufort Group, Karoo Basin, South Africa. *The Journal of Sedimentary Research*, 84(4), 326-348. https://doi.org/10.2110/jsr.2014.28

Wischmeier, W.H., Smith, D.D. 1978. *Predicting rainfall erosion losses: a guide to conservation planning* (No. 537). Department of Agriculture, Science, and Education Administration.

Yue, L., Juying, J., Bingzhe, T., Binting, C., Hang, L. (2020). Response of runoff and soil erosion to erosive rainstorm events and vegetation restoration on abandoned slope farmland in the Loess Plateau region, China. *Journal of Hydrology*, 584, 124694. https://doi.org/10.1016/j.jhydrol.2020.124694

Zengeni, R., Kakembo, V., Nkongolo, N. (2016). Historical rainfall variability in selected rainfall stations in Eastern Cape, South Africa. *South African Geographical Journal= Suid-Afrikaanse Geografiese Tydskrif*, 98(1), 118-137. https://doi.org/10.1080/03736245.2014.977811

Zhang, Y., Jiang, Y., Sun, X., Li, H., Yuan, C., Liu, H., Liu, J., Mello, C.R., Boyer, E.W., Guo, L. (2024). The hydrologic nature of swales uncovers remarkable influence of non-topographic factors on catchment-scale soil moisture variation. *Journal of Hydrology*, 635, 131196. https://doi.org/10.1016/j.jhydrol.2024.131196